Cross-property correlations and permeability estimation in sandstone

Christoph H. Arns,[1] Mark A. Knackstedt,[1,2] and Nicos S. Martys[3]
[1]*Department of Applied Mathematics, Research School of Physical Sciences and Engineering, Australian National University, Canberra ACT 0200, Australia*
[2]*School of Petroleum Engineering, University of New South Wales, Sydney, NSW 2052, Australia*
[3]*Materials and Construction Research Division, National Institute of Standards and Technology, Gaithersburg, Maryland 20899-8600, USA*

(Received 1 June 2005; revised manuscript received 10 August 2005; published 5 October 2005)

We computationally investigate cross-property correlations linking fluid permeability to conductive properties in sedimentary rock for a number of pore size parameters based on three-dimensional digitized rock images. In particular, we focus on correlations based on the pore volume-to-surface-area ratio (V_p/S), a critical channel diameter ℓ_c associated with mercury porosimetry measurements, length scales associated with the nuclear magnetic resonance relaxation time T_2, as well as the mean survival time $\langle\tau\rangle$. Differences between the length scales are discussed. All these correlations yield good agreement with our simulations, but permeability estimates based on the critical diameter ℓ_c are found to be most reliable.

DOI: 10.1103/PhysRevE.72.046304 PACS number(s): 47.55.−t, 91.60.−x, 61.43.−j

I. INTRODUCTION

A long standing and important problem in the study of flow in porous media is to relate the permeability k of a material saturated with a single fluid to other physical properties. In petroleum engineering and groundwater applications direct measurement of permeability in boreholes is impractical, and correlations to measurements of other properties such as porosity, electrical conduction [1], mercury porosimetry [2,3], and NMR response [4–6] have been used to estimate permeability [7,8]. This has led to a number of proposed relationships between fluid permeability and other properties [2,8,9]. Testing of these correlations, where all necessary parameters can be calculated, have been limited to a periodic array of spheres [10], model random sphere packs [1,11], and stochastic reconstructions of porous materials [12]. In the present paper, our aim is to examine these correlations on realistic rock morphologies derived from three-dimensional (3D) digitized tomographic images.

Permeability to fluid flow in a specified direction is given by Darcy's law

$$Q = -\frac{k}{\nu}\frac{\Delta P}{L}, \tag{1}$$

where $\Delta P = P_2 - P_1$ is the applied pressure difference across a porous sample of length L with inlet pressure P_1 and outlet pressure P_2, Q is the macroscopic volumetric flux of the fluid per unit area, and ν is the fluid viscosity. Equation (1) is analogous to Ohm's law for the flow of electric current and k is the analog of the effective conductivity. k has the dimensions of area and may be thought of as representing the cross-sectional area of an effective channel for fluid flow through the pore space. Accordingly, any estimate of k must involve an estimate of the length scale relevant to flow.

We have previously shown that accurate numerical estimates of conductivity [13] and permeability [14] can be obtained directly from simulations on 3D digitized images of sandstone. In this paper, we measure a number of pore size parameters used in the estimation of fluid permeability on the same digitized images. In particular, we focus on the pore volume-to-surface-area ratio (V_p/S), a critical channel diameter ℓ_c associated with mercury porosimetry measurements, and length scales related to restricted diffusion, namely, the NMR relaxation time T_2 as well as mean survival time $\langle\tau\rangle$ in the infinite trap problem [15]. These length scales are used in a number of theoretical and empirical correlations to estimate permeability. We perform a direct examination of cross-property correlations on the basis of the digitized images. All correlations give good agreement but estimates based on the critical diameter ℓ_c are found to be most reliable.

The organization of the paper is as follows: In the next section the theoretical background to the permeability correlations is given. In the third section we detail the numerical approach and describe the geometrical and physical measures of Fontainebleau sandstone obtained in this study. Comparisons of the different permeability correlations are given thereafter, followed by conclusions.

II. THEORETICAL SUMMARY

A. Kozeny-Carman relation

One of the earliest empirical equations for estimating permeability is the Kozeny-Carman formula

$$k = \frac{\phi(V_p/S)^2}{2\alpha}, \tag{2}$$

where V_p and S denote the volume and surface area of the pore space, respectively, and the ratio V_p/S provides a pore length scale. α defines the tortuosity of the flow channels, which is usually related to the effective resistance to electrical current flow across a fluid saturated rock σ_{eff} divided by the conductance of the fluid σ_f

$$\frac{\sigma_{\text{eff}}}{\sigma_f} = \frac{1}{F(\phi)} = \frac{\phi}{\alpha(\phi)}, \tag{3}$$

where F is commonly referred to as the formation factor.

B. Critical pore diameter

Ambegaokar *et al.* [16] considered the problem of electrical transport in networks with very wide distributions of local conductances. In such systems, it was argued that the effective conductivity of the system was controlled by the largest conductances which form percolating or spanning pathways across the network. Katz and Thompson [3] extended this approach to a description of the permeability of sedimentary rock, arguing that permeability can be correlated to ℓ_c, a critical pore diameter corresponding to the diameter of the smallest pore of the set of largest pores that percolate through the rock

$$k = \frac{c_k \ell_c^2}{F}, \tag{4}$$

where c_k is a constant that depends on the distribution of pore sizes. The value of c_k derived in [3] was $c_k \simeq 1/226$. More recent work suggest that the correct value of c_k should be larger by a factor of 2-4 [7,17]. The latter correlation was derived for systems exhibiting a very broad distribution of pore sizes. When considering a system with a narrow distribution, a single cylindrical pore type gives the classical Washburn result $c_k = 1/32$. For hyperbolic system, e.g., converging-diverging pores where one of the mean curvatures and therefore the Gaussian curvature is negative, one observes [18] $c_k \simeq 1/20$. Since the parameter c_k in Katz-Thompson varies only slowly across a broad range of pore shapes and pore size distributions, the Katz-Thompson relationship can be expected to be a fairly robust predictor of k.

A feature of this method is that ℓ_c can be directly measured from mercury intrusion experiments. Katz and Thompson [3] argue that ℓ_c is given by the position of the inflection point of the mercury intrusion curve.

C. NMR permeability correlations

The connection between NMR relaxation measurements and permeability stems from the strong effect that the rock surface has on promoting magnetic relaxation. For a single pore in the fast diffusion limit, the magnetic decay as a function of time is described by a single exponential decay [19,20]

$$M(t) = M_0(t)\exp\left[-\frac{t}{T_2}\right], \tag{5}$$

where M_0 is the initial magnetization and the transverse relaxation time T_2 is given by

$$\frac{1}{T_2} = \frac{1}{T_{2b}} + \rho\frac{S}{V_p}, \tag{6}$$

with S/V_p the surface-to-pore-volume ratio of the pore space, T_{2b} the bulk relaxation time of the fluid that fills the pore space, and ρ the surface relaxation strength. For small pores or large ρ, the bulk relaxation contribution is considered negligible and

$$\frac{1}{T_2} = \rho\frac{S}{V_p}. \tag{7}$$

Real rocks contain an assembly of interconnected pores of different sizes interconnected by pore throats which restrict diffusion. If interpore diffusion is considered negligible, each pore can be considered distinct and the magnetization within independent pores assumed to decay independently. The decay can then be described as

$$M(t) = M_0(t)\sum_{i=1}^{N} a_i \exp\left[-\frac{t}{T_{2i}}\right], \tag{8}$$

where a_i is the volume fraction of a pore i decaying with relaxation time T_{2i}. The multi-exponential distribution corresponds to a partition of the pore space into N groups based on the S/V_p values of the pores.

Permeability correlations are usually based on the logarithmic mean T_{2lm} of the relaxation time [5]

$$T_{2lm} = \exp\left[-\frac{\sum_i a_i \ln(T_{2i})}{\sum a_i}\right], \tag{9}$$

which is assumed to be related to an average V_p/S or pore size. Commonly used NMR response/permeability correlations include those of the form

$$k = a' \phi^{b'} T_{2lm}^{c'}, \tag{10}$$

with classical factors [5,7] $a'=1$, $b'=4$, $c'=2$, and

$$k = a' F^{b'} T_{2lm}^{c'}, \tag{11}$$

with standard factors $b'=-1$, $c'=2$. The latter equation with standard factors is of the same form as Eq. (2) in the fast diffusion limit.

D. Diffusion modes to permeability correlations

In this process M_0 uniformly distributed particles are allowed to diffuse randomly in the pore space with diffusion constant D_0 and removed as soon as they hit the pore-grain interface [11,21]. The signal decay can be represented by the diffusion eigenmodes

$$M(t) = M_0 \sum_{n=1}^{\infty} I_n e^{-t/\tau_n}, \ \tau_1 \geqslant \tau_2 \geqslant \tau_3 \geqslant \cdots, \tag{12}$$

where I_n and τ_n are the amplitude and lifetime associated with the nth mode. The mean survival time $\langle\tau\rangle$ is given by [11,15]

$$\langle\tau\rangle = \sum_{n=1}^{\infty} I_n \tau_n = \int_0^{\infty} \frac{M(t)}{M_0} dt, \tag{13}$$

and can thus be calculated by either a sum over the diffusion eigenmodes after an inverse Laplace transform or by the area

under the normalized relaxation curve. The fluid permeability k is related to this diffusion-limited trapping problem [11,15] and Torquato and Kim [15] proposed

$$k = \frac{\phi D_0 \langle \tau \rangle}{\alpha} = \frac{D_0 \langle \tau \rangle}{F}, \tag{14}$$

as an upper bound for permeability for a large class of structures, where D_0 is the bulk diffusion constant of the fluid. Schwartz *et al.* [11] further considered the correlation

$$k \propto \frac{\phi^2 D_0 \langle \tau \rangle}{\alpha} = \frac{\phi D_0 \langle \tau \rangle}{F}, \tag{15}$$

which they showed to be a superior correlator to permeability for sphere packs.

III. NUMERICAL SIMULATION

A microstructure defined by a digital image is already discretized and lends itself immediately to numerical computation of various properties. In this section, we describe the numerical methods used to calculate the pores size parameters, NMR response, mean survival time, and single-phase flow properties on digital images of sedimentary rock.

A. Image acquisition

The digitized pore images were obtained from 4.52 mm diameter cylindrical core samples extracted from each of four blocks of Fontainebleau sandstone with bulk porosity ϕ=7.5%, 13%, 15%, and 22%. A 2.91 mm length of each core was imaged [22,23]. The reconstructed images have a resolution of 5.7 μm resulting in $795 \times 795 \times 512$ imaged sections. Each grey scale image was thresholded using a kriging-based thresholding method [24] to give a binary pore-solid image [25]. From each original cylindrical plug we extract a 480^3 cubic subset for analysis corresponding to a volume of $(2.73\ \text{mm})^3$.

B. Choice of representative sample size

When minimizing finite size errors one must ensure that the size of the system compared to some statistical length scale (e.g., correlation length, mean grain size) is large. Errors will occur if one uses too few voxels in simulating a property. Optimally, we would choose a system size which has an acceptable finite size error, but is still small enough to allow computational prediction of properties. Previous work on Fontainebleau sandstone has shown that simulations of petrophysical properties of Fontainebleau sandstone at a scale of $(700\ \mu\text{m})^3$ were in reasonable agreement with predictions on larger cells [13,14,26,27]. This relatively small sample size allows one to take 64 independent 120^3 samples from each Fontainebleau image at 480^3. The variation in porosity across the four samples as well as the subsections of each sample result in a full property:porosity $(k/F/T_2/\langle\tau\rangle:\phi)$ relationship across a range of ϕ rather than a single data point. In the remainder of this paper, all cross correlations between properties are based on this sample size (120^3). Pore size distribution data are given on the full 480^3 samples.

C. Geometrical length measures

From a single 3D digital image one can directly measure a range of morphological parameters including $\phi, V_p/S$ and pore size distributions. ϕ and V_p/S are evaluated by simple counting of the numbers of voxels and faces on the image [28,29]. This counting method can overpredict the surface area; e.g., for a digital sphere the correction is about 1.5 [30] (see also the correction factor used in the NMR simulations).

1. Maximal inscribed spheres

One technique for measuring the pore size information is based on a classical mathematical description of the morphology in terms of basic geometrical quantities [31]. More complete and generic descriptions of the basic concepts and techniques are given elsewhere [32,33]. We define in particular the covering radius for each point in the pore phase—this corresponds to an opening size in the standard mathematical morphology.

The dilation of a pore phase domain A by a spherical (circular in 2D) element B of radius R is the set covered by all translations of B_R centered in A

$$A \oplus B_R = \cup_{r \in A, s \in B_R} (\mathbf{r} + \mathbf{s}). \tag{16}$$

The erosion is the dual operation corresponding to dilation of the complement A^c of A and corresponds to all points in A not covered by a sphere B_R centered out of A via

$$A \ominus B_R = (A^c \oplus B_R)^c. \tag{17}$$

The morphological opening $\mathcal{O}$ of a geometrical object A by a sphere of radius R is the domain swept out by all the translates of R that lie within A [31]

$$\mathcal{O}_R(A) = (A \ominus B_R) \oplus B_R. \tag{18}$$

$\mathcal{O}_R(A)$ is the set of points in A that can be covered by a sphere of radius R contained in A. Opening filters out small convexities and removes smaller isolated clusters. A size $r_c(\mathbf{r})$ can be associated with any point in A, defined as the radius of the largest sphere contained in A that covers $\mathbf{r}$. In the language of [33]

$$r_c(\mathbf{r}) = \sup[R{:}\mathbf{r} \in \mathcal{O}_R(A)]; \tag{19}$$

$r_c(\mathbf{r})$ is defined as the covering radius of $\mathbf{r}$. The cumulative pore size distribution is then defined with respect to the radius R

$$F(R) = \frac{\text{Vol}[\mathcal{O}_R(A)]}{\text{Vol}[A]}, \tag{20}$$

where Vol denotes the volume of the argument.

Figures 1(a) and 1(b) illustrate the concept for a two dimensional example. Figure 1(c) depicts the point where covering spheres of $r \geq r_c$ first form a connected vertical pathway across the medium. In the language of mathematical morphology, Fig. 1(c) illustrates the point, where the domain

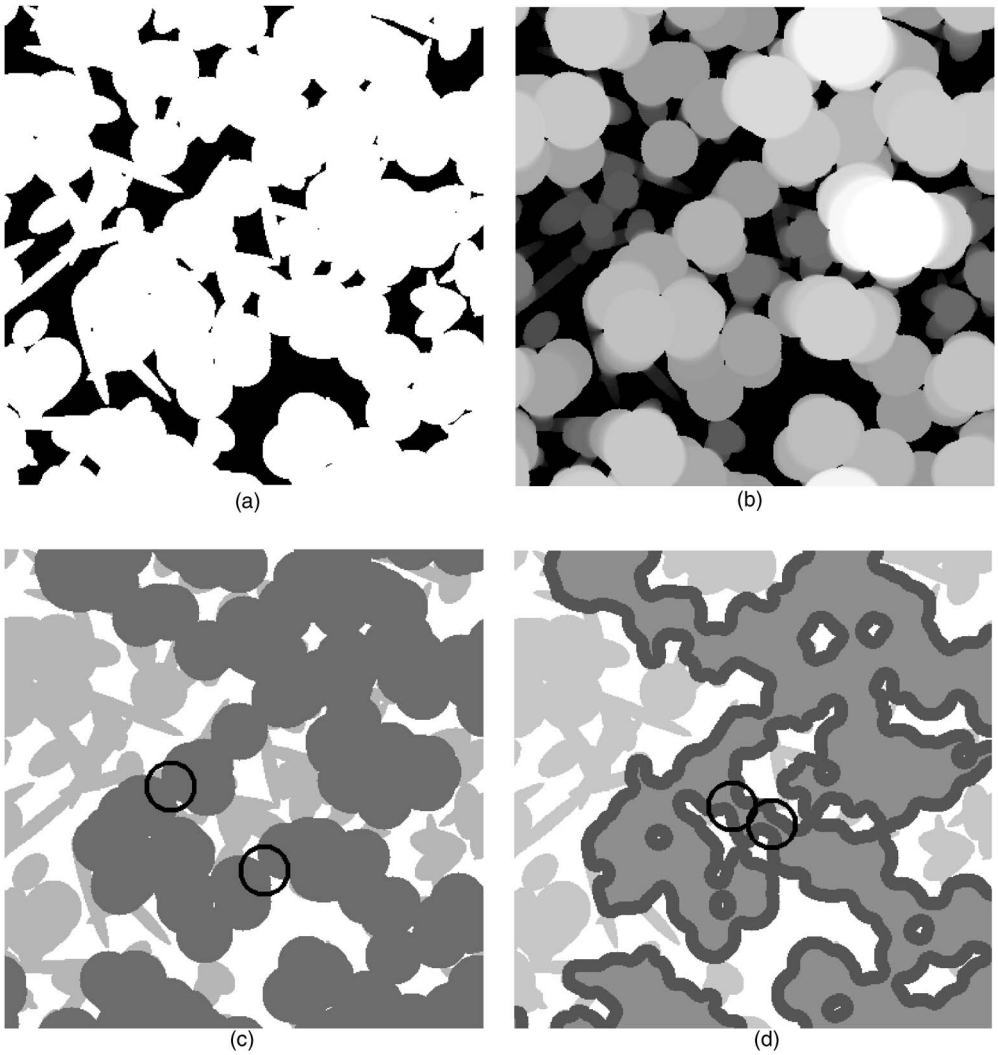

FIG. 1. Illustration of the measurement of the covering radius for the pore size distribution and ℓ_c. In (a) a model complex 2D media is shown; all simulations reported in the paper are performed in 3D. (b) shows the corresponding field of covering radii $r_c(\mathbf{r})$ of the white phase in (a) with the grey scale proportional to covering disk radius. (c) shows the covering radii for all $r \geq r_c$ for connectivity in the vertical direction. (d) illustrates the covering radii defined by ℓ_c in the vertical direction. The circles in (c) and (d) highlight the different critical pathways which form within the spanning cluster at breakthrough.

defined by $(A \ominus B_{R_c}) \oplus B_{R_c}$ first percolates. Figure 2(a) shows the pore size distribution defined by the covering radius for the four 480^3 sandstone tomograms.

2. Capillary pressure and ℓ_c

ℓ_c is associated with the diameter of the largest sphere which can percolate across the pore system and is defined by the percolation threshold of a nonwetting phase penetrating the pore space during a drainage (e.g., mercury porosimetry) experiment. To model this, one must slightly modify the algorithm to measure r_c and determine the diameter ℓ_c of the largest sphere which can *pass through* the porous medium [32]. The result of this process is illustrated in Fig. 1(d). Note that the connected pathway at ℓ_c follows a different route to the connected pathway defined by the maximal sphere radius R_c and that $R_c > \ell_c$. This subtle difference is due to spheres connecting across narrow throats (see Fig. 14 of [32]); in a drainage experiment the meniscus cannot pass through this narrow throat while the covering radius connects across the throat. In the language of mathematical morphology the connected cluster is defined when $(A \ominus B_{\ell_c})$ first percolates. The resultant domain after opening is given by $(A \ominus B_{\ell_c}) \oplus B_{\ell_c}$ [34]. One can simulate a complete digital mercury intrusion capillary pressure curve by considering all possible invading sphere radii ([32]). Katz and Thompson [3] argued that ℓ_c can be measured from mercury intrusion measurements. The maxima of the pore size distribution from simulated mercury intrusion agree well with the values of ℓ_c [Fig. 2(b)]. In Table I we review the values ℓ_c and compare to the other length measures used in this paper.

D. D. NMR response

The spin relaxation in the NMR response of a saturated porous system is simulated by using a random walk method; the Brownian motion of a diffusing magnetized particle is simulated. Initially, the walkers are placed randomly in the 3D pore space. At each time step the walkers are moved from their initial position to a neighboring site and the clock of the walker advanced by $\Delta t = \epsilon^2/(6D_0)$, where ϵ is the lattice spacing and D_0 the bulk diffusion constant of the fluid, reflecting Brownian dynamics. An attempt to go to a closed site will kill the walker with probability $\gamma/6, 0 \leq \gamma \leq 1$ [35]. The killing probability γ is related to the surface relaxivity ρ, a phenomenological parameter quantifying the strength of surface-enhanced relaxation [6,36], via

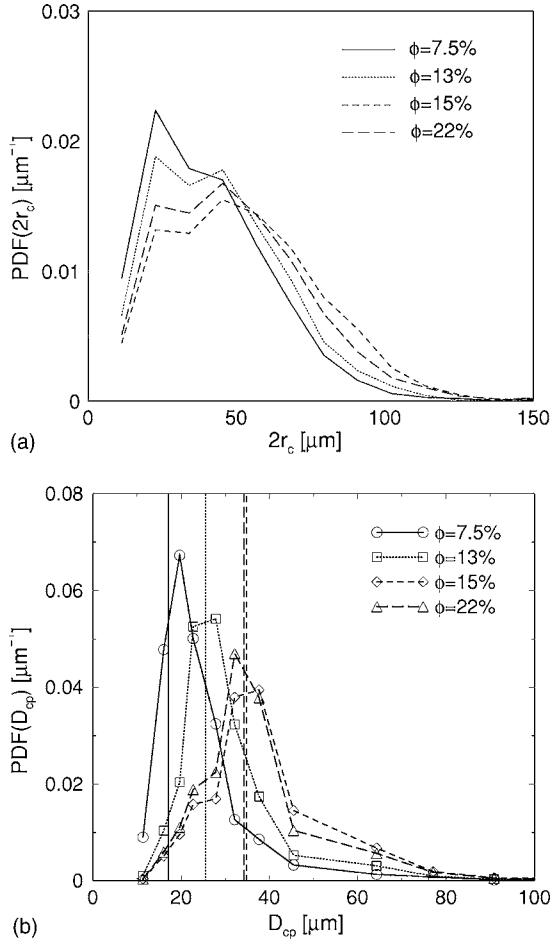

FIG. 2. Probability density functions of pore diameter (a) by the maximal sphere algorithm ($2r_c$) and (b) derived from a drainage simulation (Ref. [32]). The vertical bars in (b) indicate the position of l_c and coincide reasonably with the maxima of the curves (within voxel accuracy).

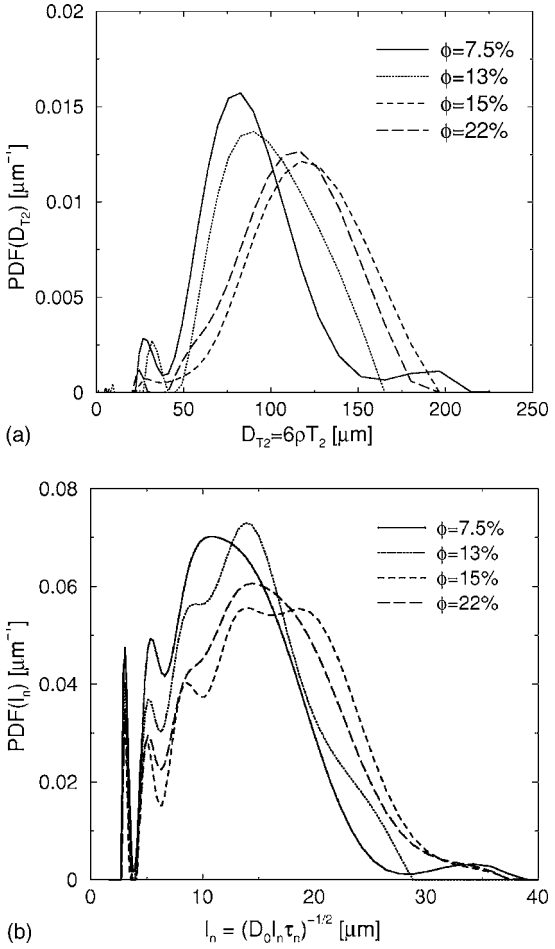

FIG. 3. Probability density functions of diffusion length scales. (a) pore diameter inferred from inversion of NMR relaxation data under the assumptions of fast diffusion and spherical pores. (b) spectrum of eigenmodes contributing to the first passage length scale [see Eqs. (12) and (13)].

$$A\gamma = \frac{\rho\epsilon}{D_0} + O\left[\left(\frac{\rho\epsilon}{D_0}\right)^2\right], \tag{21}$$

[21,37,38]. Here A is a correction factor of order 1 accounting for the details of the random walk implementation; we use $A=3/2$ [38]. If the walker survives it bounces off the interface (returns to the previous position), and time is advanced by the time step Δt. By repeating this procedure for a large number of walkers, the life time distribution of random walkers is generated. This distribution is used to calculate the magnetization amplitude as a function of time. The relaxation time distribution is obtained by fitting a multiexponential decay to $M(t)$, using bounded least squares [39] combined with Tikhonov regularization [40,41]. The optimal regularization parameter is chosen by the corner of the L-curve method [42] on the unconstrained problem. All routines were implemented in FORTRAN95 and use the LAPACK library where appropriate.

TABLE I. Comparison of different length scales derived on the tomograms. d_{VS}, d_{rc}, and d_{lc} are morphological measures, d_{T2} and d_τ diffusive length scales. ℓ_c is obtained in three orthogonal directions and an average reported. All values are in micrometers.

ϕ	7.5%	13%	15%	22%
$d_{VS}=6V_p/S$	64.9	75.0	90.6	85.9
$d_{rc}=2\bar{r}_c$	40.7	44.7	53.4	50.1
$d_{lc}=\bar{\ell}_c$	17.3	25.4	34.7	34.1
$d_{T2}=6\rho T_{2lm}$	73.9	84.5	103.4	97.4
$d_\tau=6\sqrt{D_0\langle\tau\rangle}$	68.9	74.1	87.5	83.4

We used $\rho=16$ μm/s [36,43,44] and $D_0=2500$ μm^2/s, resulting in $\gamma=0.0242$, to simulate the NMR response. In Fig. 3, we plot the resultant pore size distribution ($d_{T2}=6\rho T_2$) from simulation of the NMR response and an inverse Laplace transform. The pore diameters calculated from the logarithmic mean T_{2lm} for the four cores $d_{T2}=6\rho T_{2lm}$ are slightly larger than the value of d_{VS} (see Table I); this implies that for the choice of ρ on this morphology we lie slightly outside the fast diffusion limit. Comparing the distributions of Figs. 2 and 3 we note that the algorithm based on maximal inscribed spheres gives pore

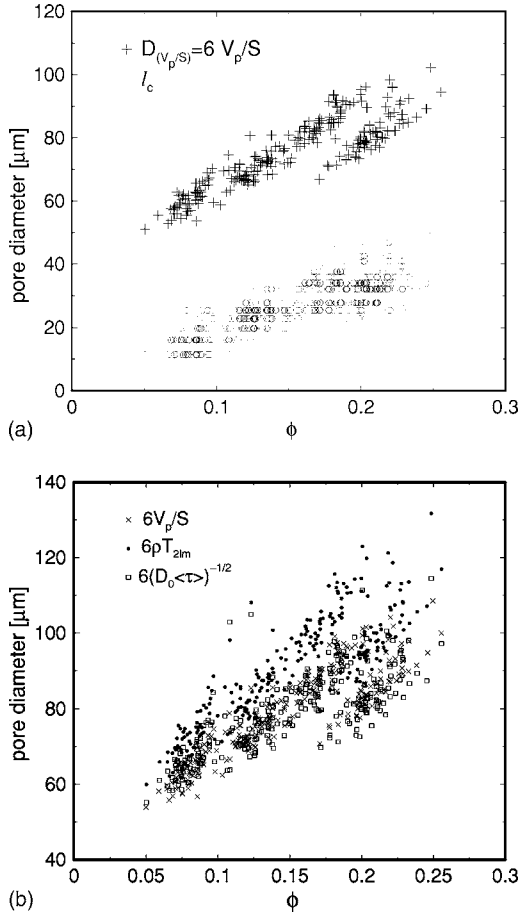

FIG. 4. Length scales d_{VS}, d_{T2}, and ℓ_c derived directly on images. In (a) we compare d_{VS} and ℓ_c, and in (b) show that the variation in d_{VS} versus the diffusive length scales d_{T2} and d_τ is minimal.

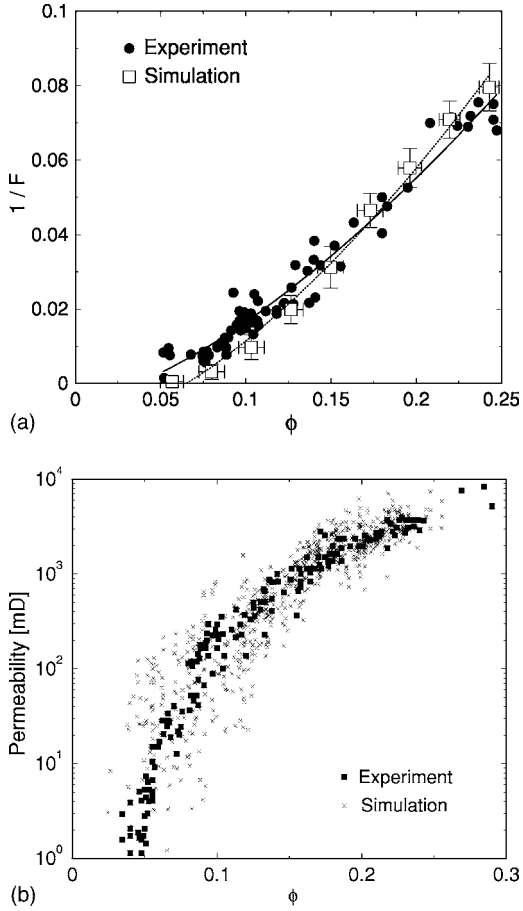

FIG. 5. Comparison of the numerical prediction of the (a) electrical conductivity and (b) permeability simulations for the Fontainebleau sandstone with experimental data. The lines in (a) indicate best fits to the experimental data (solid line) and numerical data (dotted line).

sizes smaller than the algorithm based on T_2. This is expected since the NMR signal decay is related to a structural length V_p/S defined for all shapes of pores while the maximal sphere gives a measure based on assumed spherical symmetry. For example, a long cylindrical pore would have just one structural length given by $r/2$, while for covering spheres one gets $r/3$. Further, d_{T2} is determined by the larger pore volumes, while ℓ_c is thought to be [3] associated with the pore throats and is much smaller than d_{T2}. Similar trends are observed when comparing d_{T2}, d_{VS}, and ℓ_c on all 256×120^3 subsets of the four cores (Fig. 4).

E. Mean survival time

The calculation of the mean survival time is a special case of the NMR routines described above. The same random walk routines are used, but with $\gamma=1$, i.e., infinitely deep traps resulting in the slow diffusion limit. The mean survival time is calculated by both methods suggested in Eq. (13), namely, either a sum over the eigenvalues after an inverse Laplace transform or as an integral over the relaxation curve. The relative differences for $\langle\tau\rangle$ between the methods are under 1%.

The spectrum of diffusion eigenmodes contributing to the first passage length scale for the full samples is shown in Fig. 3(b). Table I compares the equivalent sphere diameter derived from the first passage time to the other length scales. The difference between d_{VS} and d_τ is small. Figure 4(b) compares for the 120^3 subsets the first passage length scale to the structural length scale d_{VS} and the NMR relaxation length scale d_{T2}. Again, the difference between d_{VS} and d_τ is small over the full porosity range.

F. Electrical conductivity

The conductivity calculation is based on a solution of the Laplace equation with charge conservation boundary conditions. The three-dimensional voxel microstructure is first converted into a network of resistors by connecting each pair of adjacent voxels by a resistor. A potential gradient is applied in each coordinate direction, and the system relaxed using a conjugate gradient technique to evaluate the field. We assign to the matrix phase of the sandstone a conductivity $\sigma_{\text{mineral}}=0$ and to the (fluid-filled) pore phase a normalized conductivity $\sigma_{\text{fl}}=1$. The conductivity is scaled to continuum values by determining a scaling factor as a function of porosity by the technique detailed in [13].

The formation factor, the ratio of the measured conductance of the fluid filled rock σ_{eff} to that of the fluid itself,

given by $F=\sigma_{fl}/\sigma_{eff}$, is reported. The best fit to the conductivity simulation for all cores gives for the formation factor $F=0.432\ \phi^{-2.29}$ [Fig. 5(a)] and accordingly for tortuosity $\alpha=0.432\ \phi^{-1.29}$.

G. Permeability simulation

The permeability calculation is based on a lattice-Boltzmann method (LB) using D3Q19 (three-dimensional lattice with 19 possible momenta components) [45]. The implementation of the algorithm is similar to that detailed by [46]. The physical boundary condition at solid-fluid interfaces is the no-flow condition which in the LB methods is most simply realized by the bounce-back rule [47]. The pressure gradient acting on the fluid is simulated by a body force [48]. Mirror image boundary conditions [46] are applied in the plane perpendicular to the flow direction and all simulations were performed on a $L\times L\times 2L$ system; permeability is

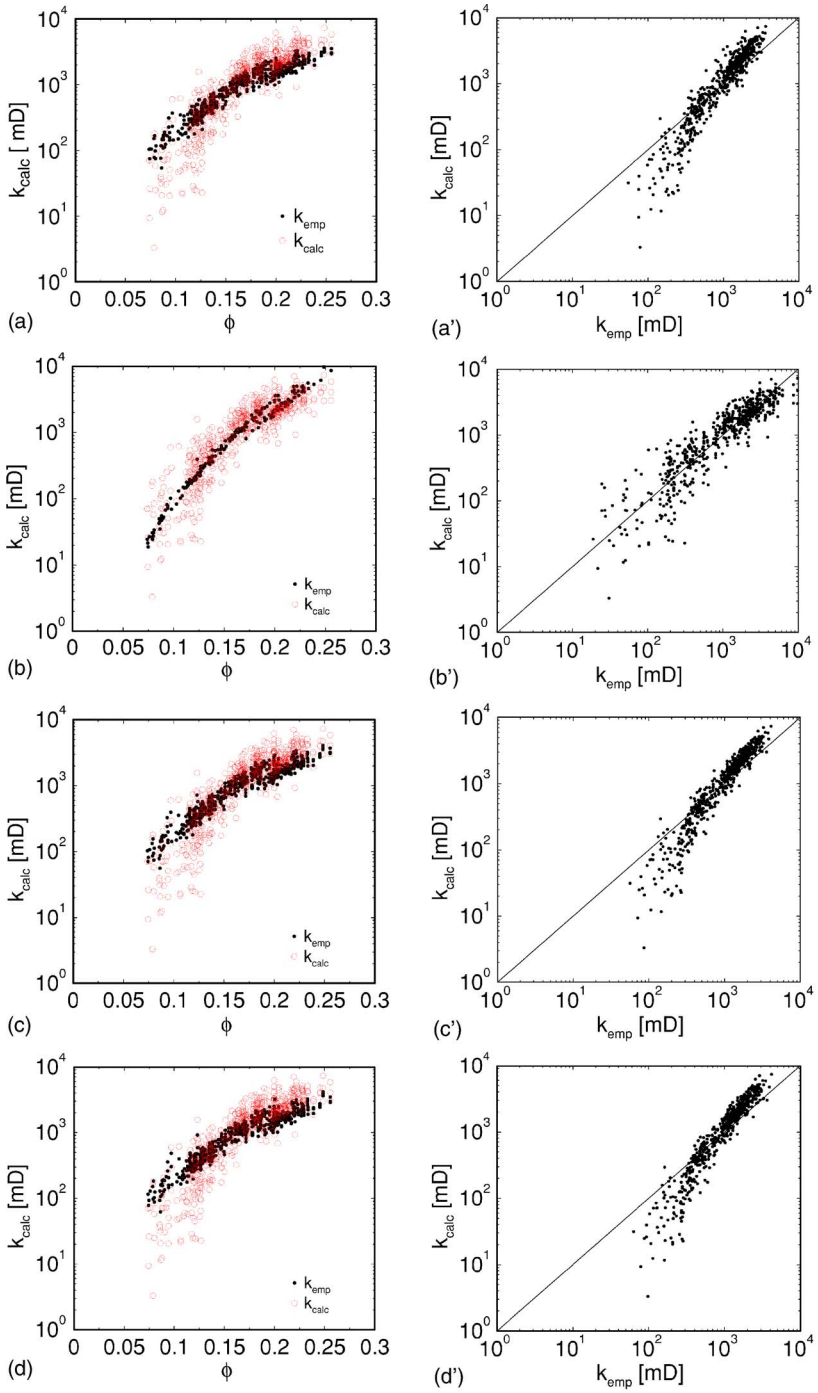

FIG. 6. (Color online) Permeability estimators using one-parameter fits. (a) Kozeny-Carman, (b) NMR T_2, Eq. (10), (c) NMR T_2, Eq. (11), (d) first passage time, Eq. (14), (e) first passage time, Eq. (15), and (f) critical path estimator. The right column shows associated cross-plots [(a′)–(f′)].

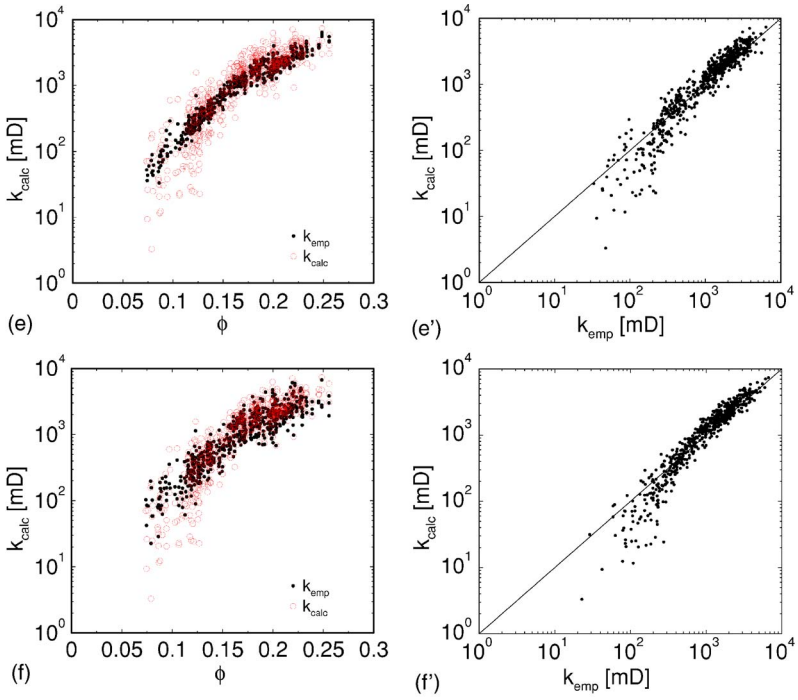

FIG. 6. (*Continued*).

measured in the central (L^3) subset. In all cases, the LB relaxation parameter $\tau_{\mathrm{LB}}=1$ is used. All values of k are reported in milliDarcys [mD] (1 Darcy$=0.98692\times10^{-12}$ m^2).

Data obtained for conductivity [13] and permeability [14] are summarized in Fig. 5(b) and compared to experimental data.

IV. PERMEABILITY CORRELATIONS

The computation of $k, F, T_2, \langle\tau\rangle, V_p/S, \ell_c$ across three orders of magnitude in permeability on 256 independent samples offers an opportunity to test the commonly applied permeability correlations in a controlled fashion. The correlations for k discussed in section two [Eqs. (2), (4), (10), (11), (14), and (15)] can be written as a function of a length scale d_{len}, a porosity exponent b, and a tortuosity exponent c according to

$$k = a\phi^b\alpha^c d_{\mathrm{len}}^2, \tag{22}$$

where d_{len} can be d_{VS}, d_{T2}, d_τ, or ℓ_c. In all fits to the 256 independent samples the mean residual error

$$s^2 = \frac{\sum[\log_{10}(k_{\mathrm{calc}}) - \log_{10}(k_{\mathrm{emp}})]^2}{n-2}. \tag{23}$$

is minimized and the correlation coefficient

$$R = \frac{\sum(k_{\mathrm{emp}} - \overline{k_{\mathrm{emp}}})(k_{\mathrm{calc}} - \overline{k_{\mathrm{calc}}})}{\left[\sum(k_{\mathrm{emp}} - \overline{k_{\mathrm{emp}}})^2(k_{\mathrm{calc}} - \overline{k_{\mathrm{calc}}})^2\right]^{1/2}} \tag{24}$$

calculated. Here ℓ_c, α, and k are considered in the three coordinate axes directions, resulting in three times the number of data points.

A. Single parameter fits to classical equations

Here we fit the prefactor a in Eq. (22) and use the classical values for the exponents given by Eqs. (2), (4), (10), (11), (14), and (15). The results are given in Fig. 6 and Table II.

The best fit for $a(=0.00394)$ in the Kozeny-Carman relationship is plotted in Figs. 6(a) and 6(a′) [$R=0.917$, $s^2=0.0943$]. Neither the trend of the data nor the variability is very well captured. In Figs. 6(b) and 6(b′) we show the prediction of Eq. (10) (NMR T_2) with standard factors $b=4$, $c=0$ [$R=0.85$, $s^2=0.082$]. While the residual error is relatively small, the prediction does not exhibit the wide spread in k for each ϕ and the correlation coefficient is relatively poor. Figures 6(c) and 6(c′) show the prediction of Eq. (11) for NMR T_2 with a single parameter fit [$b=1$, $c=-1$, $R=0.95$, $s^2=0.0.090$]. The residual is quite large, but the correlation coefficient is improved and the variability at similar ϕ of the permeability is better captured. Despite be-

TABLE II. Summary of coefficients used in the one-parameter-fit permeability correlations. Each set of coefficients resulted in a permeability estimate which is compared to the simulated permeability. The quality of the fit for all correlations is given.

Empirical estimate	a	R	s^2
$k=a\phi\alpha^{-1}d_{VS}^2$	0.00394	0.917	0.0943
$k=a\phi^4 d_{T2}^2$	0.145	0.846	0.0818
$k=a\phi\alpha^{-1}d_{T2}^2$	0.00302	0.951	0.0897
$k=a\phi\alpha^{-1}d_\tau^2$	0.00407	0.941	0.0975
$k=a\phi^2\alpha^{-1}d_\tau^2$	0.0251	0.928	0.0666
$k=a\phi\alpha^{-1}\ell_c^2$	0.0331	0.953	0.0621

TABLE III. Summary of coefficients used in the two- and three-parameter fit permeability correlations. Each set of coefficients resulted in a permeability estimate which is compared to the simulated permeability. The quality of the fit for all correlations is given.

Empirical estimate	a	b	c	R	s^2	Fit
$k=a\phi^b\alpha^c d_{VS}^2$	0.0664	2.55	−1	0.898	0.0624	a,b
	0.0269	1	−2.21	0.942	0.0507	a,c
	0.0181	0.542	−2.49	0.945	0.0502	a,b,c
$k=a\phi^b\alpha^c d_{T2}^2$	0.112	3.86	0	0.850	0.0816	a,b
	0.0467	2.50	−1	0.924	0.0596	a,b
	0.264	4	−.376	0.861	0.0776	a,c
	0.0197	1	−2.18	0.967	0.0479	a,c
	0.0127	0.491	−2.49	0.970	0.0473	a,b,c
$k=a\phi^b\alpha^c d_\tau^2$	0.0839	2.66	−1	0.912	0.0608	a,b
	0.0315	1	−2.29	0.961	0.0480	a,c
	0.0747	2	−1.69	0.940	0.0526	a,c
	0.0216	0.567	−2.55	0.964	0.0475	a,b,c
$k=a\phi^b\alpha^c \ell_c^2$	0.202	1.99	−1	0.949	0.0490	a,b
	0.111	1	−1.76	0.957	0.0448	a,c
	0.0936	0.806	−1.88	0.956	0.0447	a,b,c

ing almost identical to the form of the Kozeny equation, slight deviations from the fast diffusion limit are noted and the fit is slightly better. Figures 6(d) and 6(d′) display permeability correlations given by Eq. (14) [$a=0.00407$, $b=1$, $c=-1$, $R=0.941$, $s^2=0.097$]. The one-parameter fit leads to a good estimate of permeability, but does not capture the permeability trend at the low-porosity end of the curve. The second correlation involving d_τ [Eq. (15)], plotted in Figs. 6(e) and 6(e′), gives a lower residual error but poorer correlation coefficient [$a=0.0251$, $b=2$, $c=-1$, $R=0.928$, $s^2=0.666$]. Previous work for a sphere pack [11] showed a better correlation for Eq. (15) versus Eq. (14); here the case is not clear. In Figs. 6(f) and 6(f′) we show the prediction of Eq. (4) using the critical sphere diameter ℓ_c [$R=0.953$, $s^2=0.062$] and the error in the prediction. The single parameter fit matches both the permeability trend with porosity as well as the variability of the data reasonably well.

B. Fits to classical equations with varying exponents

The two- and three-parameter fits apply the downhill simplex method *amoeba* [49]. All two-parameter fits optimize the prefactor a and either the porosity exponent b or the tortuosity exponent c. Results of all correlations involving two or three parameters are summarized in Table III and Fig. 7. Of the two-parameter fits changing the tortuosity exponent c gives a much better fit to the data than changing the porosity exponent b. All best two-parameter fits give a good fit to the data (Fig. 7). Three-parameter fits do not significantly reduce the residual or increase the correlation coefficient (see Table III).

The fit to the Kozeny-Carman relationship with varying tortuosity exponent is shown in Figs. 7(a) and 7(a′). Now the permeability-porosity trend of the data is captured correctly. Figures 7(b) and 7(b′) show the best two-parameter fit of Eq. (11) [$a=0.0197$, $b=1$, $c=-2.18$, $R=0.967$, $s^2=0.048$]. Again, the inclusion of the tortuosity exponent leads to lower variability of the permeability and a good trend with porosity. The quality of the two-parameter fits are consistent with coefficients given from permeability correlations derived from stochastic reconstructions of Fontainebleau sandstone [43]. Figures 7(c) and 7(c′) present the best two-parameter fit involving the prefactor and a tortuosity exponent [$a=0.0315$, $b=1$, $c=-2.29$, $R=0.961$, $s^2=0.0480$] for the permeability-first passage time predictor. While the one-parameter fits did not capture either the permeability trend at the low-porosity end of the curve or the variability, again adding a tortuosity parameter results in an excellent fit. The data in Table III shows that the porosity exponent $b=1$ according to Eq. (14) is clearly favorable to $b=2$ of Eq. (15). In Figs. 7(d) and 7(d′) we show the best match from a two-parameter fit according to Eq. (22) involving the critical sphere radius ℓ_c [$a=0.111$, $b=1$, $c=-1.76$, $R=0.957$, $s^2=0.0448$]. While a one-parameter fit to the data worked reasonably well, use of a two-parameter fit including a tortuosity parameter significantly improved the fit, while the three-parameter fit (see Table III) leads to marginal further improvement.

V. CONCLUSIONS

From the visual inspections of Figs. 6 and 7 and results summarized in Tables II and III we make the following conclusions:

1. The most appropriate length scale for the prediction of the permeability of Fontainebleau sandstone is ℓ_c. This is a reflection of the fact that permeability is mainly determined by the size of pore throats and ℓ_c is associated with the percolation threshold of a nonwetting phase penetrating the pore space during a drainage process; this is dependent on critical throat radii. NMR permeability correlations do not

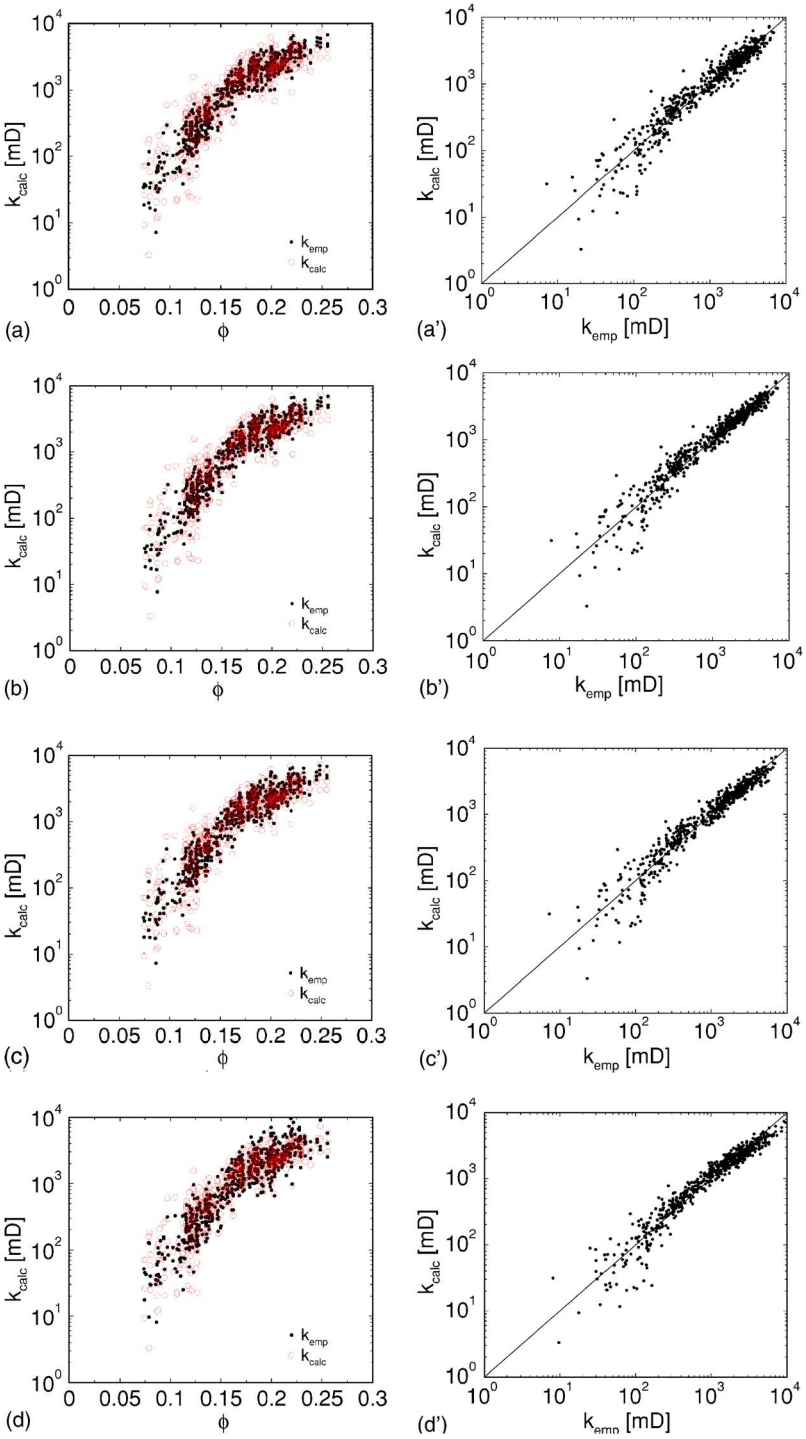

FIG. 7. (Color online) Permeability estimators using best two-parameter fits. (a) Kozeny-Carman, (b) NMR T_2, (c) first passage time, and (d) critical path estimator and associated cross plots [(a′)–(d′)].

perform as well, but still show a remarkably good fit to the data. This suggests that throat sizes are strongly correlated to pore sizes in this sandstone. The results for V_p/S correlate strongly to T_{2lm}.

2. The most appropriate tortuosity parameter is the formation factor. Comparing predictions of Eq. (10) to Eq. (11) we see that the tortuosity defined in Eq. (3), $1/(F\phi)$, is replaced by ϕ^3. This implies that $F=\phi^{-4}$ would hold. We find the best fit to the $\ln(F):\ln(\phi)$ relationship given by $F \propto \phi^{-2.3}$ (see Sec. III F). Only at lower porosities does one observe a shift to larger exponents. This may account for the poorer fit of the data to Eq. (10). We also note that the use of F for tortuosity leads to a more representative spread of the permeability data for constant ϕ.

3. The sandstone morphology studied here is fairly homogeneous. The acquisition of tomographic data for a range of lithologies is ongoing [50–52]—this should allow more rigorous testing of the correlations discussed here for general lithologies.

We note that most reservoir sandstones contain significant clay fractions; this is true even for relatively homogeneous sands like Berea [53]. The effect of clays will strongly affect

the predictions of F and T_2. It will be important to study correlations in the presence of clays and we intend to do so in a future study.

ACKNOWLEDGMENTS

M.A.K. and C.H.A. acknowledge the Australian Government for its support through the Australian Research Council (ARC) grant scheme (DP0345886, DP0558185). M.A.K. also thanks the Australian Partnership for Advanced Computing (APAC) for its support through the expertise program and the Cooperative Reseach Centre (CRC) for Functional Communication Surfaces (FCS), BHP-Billiton and Statoil Research who have provided financial support for the project. N.S.M. thanks the HYPERCON program at NIST for partial financial support. We thank the A.N.U. Supercomputing Facility and APAC for very generous allocations of computer time.

[1] P.-Z. Wong, J. Koplik, and J. P. Tomanic, Phys. Rev. B **30**, 6606 (1984).
[2] A. J. Katz and A. H. Thompson, Phys. Rev. B **34**, 8179 (1986).
[3] A. J. Katz and A. H. Thompson, J. Geophys. Res. **92**, 599 (1987).
[4] W. E. Kenyon, P. Day, C. Straley, and J. Willemsen, in *Proceedings 61st Annual Technical Conference and Exhibition* (SPE 15643, New Orleans, 1986).
[5] W. E. Kenyon, P. Day, C. Straley, and J. Willemsen, SPE Form. Eval. **3**, 626 (1988).
[6] W. E. Kenyon, Nucl. Geophys. **6**, 153 (1992).
[7] J. R. Banavar and L. M. Schwartz, Phys. Rev. Lett. **58**, 1411 (1987).
[8] P. N. Sen, C. Straley, W. E. Kenyon, and M. S. Whittingham, Geophysics **55**, 61 (1990).
[9] D. L. Johnson, J. Koplik, and L. M. Schwartz, Phys. Rev. Lett. **57**, 2564 (1986).
[10] K.-J. Dunn, G. A. LaTorraca, and D. J. Bergman, Geophysics **64**, 470 (1999).
[11] L. M. Schwartz, N. Martys, D. P. Bentz, E. J. Garboczi, and S. Torquato, Phys. Rev. E **48**, 4584 (1993).
[12] I. Hidajat, M. Singh, J. Cooper, and K. K. Mohanty, Transp. Porous Media **48**, 225 (2002).
[13] C. H. Arns, M. A. Knackstedt, W. V. Pinczewski, and W. B. Lindquist, Geophys. Res. Lett. **28**, 3361 (2001).
[14] C. H. Arns, M. A. Knackstedt, W. V. Pinczewski, and N. Martys, J. Pet. Sci. Eng. **45**, 41 (2004).
[15] S. Torquato and I. C. Kim, J. Appl. Phys. **72**, 2612 (1992).
[16] V. Ambegaokar, B. Halperin, and J. S. Langer, Phys. Rev. B **4**, 2612 (1971).
[17] P. Le Doussal, Phys. Rev. B **39**, 4816 (1989).
[18] R. B. Saeger, L. E. Scriven, and H. T. Davis, Phys. Rev. A **44**, 5087 (1991).
[19] R. C. Wayne and R. M. Cotts, Phys. Rev. **151**, 264 (1966).
[20] K. R. Brownstein and C. E. Tarr, Phys. Rev. A **19**, 2446 (1979).
[21] D. J. Wilkinson, D. L. Johnson, and L. M. Schwartz, Phys. Rev. B **44**, 4960 (1991).
[22] J. H. Dunsmuir, S. R. Ferguson, and K. L. D'Amico, Inst. Phys. Conf. Ser. **121**, 257 (1991).
[23] P. Spanne, J. F. Thovert, C. J. Jacquin, W. B. Lindquist, K. W. Jones, and P. M. Adler, Phys. Rev. Lett. **73**, 2001 (1994).
[24] W. Oh and W. B. Lindquist, IEEE Trans. Pattern Anal. Mach. Intell. **21**, 590 (1999).
[25] W. B. Lindquist, A. Venkatarangan, J. Dunsmuir, and T. F. Wong, J. Geophys. Res. **105B**, 21509 (2000).
[26] F. M. Auzerais, J. Dunsmuir, B. B. Ferrèol, N. Martys, J. Olson, T. S. Ramakrishnan, D. H. Rothman, and L. M. Schwartz, Geophys. Res. Lett. **23**, 705 (1996).
[27] C. H. Arns, M. A. Knackstedt, W. V. Pinczewski, and E. G. Garboczi, Geophysics **67**, 1396 (2002).
[28] H. Bieri and W. Nef, Comput. Vis. Graph. Image Process. **28**, 166 (1984).
[29] C. H. Arns, M. A. Knackstedt, W. V. Pinczewski, and K. R. Mecke, Phys. Rev. E **63**, 031112 (2001).
[30] N. Martys and E. J. Garboczi, Phys. Rev. B **46**, 6080 (1992).
[31] J. Serra, *Image Analysis and Mathematical Morphology*, Vols. 1,2 (Academic Press, Amsterdam, 1982).
[32] M. Hilpert and C. T. Miller, Adv. Water Resour. **24**, 243 (2001).
[33] J.-F. Thovert, F. Yousefian, P. Spanne, C. G. Jacquin, and P. M. Adler, Phys. Rev. E **63**, 061307 (2001).
[34] A detailed simulation of mercury intrusion is more complex because it entails the determination of the local curvature of the mercury interface and an understanding of the mercury contact line. This is discussed in [32].
[35] K. S. Mendelson, Phys. Rev. B **41**, 562 (1990).
[36] M. D. Hürlimann, K. G. Helmer, L. L. Latour, and C. H. Sotak, J. Magn. Reson., Ser. A **111**, 169 (1994).
[37] K. S. Mendelson, Phys. Rev. B **47**, 1081 (1993).
[38] D. J. Bergman, K.-J. Dunn, L. M. Schwartz, and P. P. Mitra, Phys. Rev. E **51**, 3393 (1995).
[39] P. Stark and R. Parker, Comput. Stat. Data Anal. **10**, 129 (1995).
[40] C. L. Lawson and R. J. Hansen, *Solving Least Squares Problems* (Prentice-Hall, Englewood Cliffs, NJ, 1974).
[41] P. C. Hansen, Inverse Probl. **8**, 849 (1992).
[42] P. C. Hansen, SIAM Rev. **34**, 561 (1992).
[43] P. E. Øren, F. Antonsen, H. G. Rueslåtten, and S. Bakke, presented at the *SPE 77th Annual Technical Conference and Exhibition* (Soc. Pet. Eng., San Antonio, 2002).
[44] C. H. Arns, Physica A **339**, 159 (2004).
[45] Y.-H. Qian and Y. Zhou, Europhys. Lett. **42**, 359 (1998).
[46] N. S. Martys, J. G. Hagedorn, D. Goujon, and J. E. Devaney, Proc. SPIE **309**, 205 (1999).
[47] N. S. Martys and H. Chen, Phys. Rev. E **53**, 743 (1996).
[48] B. Ferreol and D. H. Rothman, Transp. Porous Media **20**, 3 (1995).
[49] W. H. Press, S. A. Teukolsky, W. T. Vetterling, and B. P. Flannery, *Numerical Recipes in Fortran 90-The Art of Parallel Scientific Computing*, Vol. II (Cambridge University Press,

Cambridge, 1996).
[50] C. H. Arns, F. Bauget, A. Ghous, A. Sakellariou, T. J. Senden, A. P. Sheppard, R. M. Sok, and W. V. Pinczewski, Petrophysics **46**, 260 (2005).
[51] C. H. Arns, H. Averdunk, F. Bauget, A. Sakellariou, T. Senden, A. Sheppard, R. Sok, W. Pinczewski, S. Bakke, L. I. Berg, *et al.*, in Presented at the *SPE 79th Annual Technical Conference and Exhibition* (Society of Petroleum Engineering, Houston, 2004), to appear in SPE, December 2005.
[52] V. H. Nguyen, A. P. Sheppard, M. A. Knackstedt, and W. V. Pinczewski, in *2004 SPE International Petroleum Conference* (Society of Petroleum Engineering, Puebla, Mexico, 2004), pp. 90365:1–21.
[53] P.-E. Øren and S. Bakke, J. Pet. Sci. Eng. **39**, 177 (2003).